

Structural Properties of Iron/Titanium Oxide Nanoparticles Synthesized by Sol-gel Method in the Presence of Poly(ethylene glycol)

Ivan Marić,¹ Marijan Gotić,^{2,*} Tanja Jurkin,¹ Lara Mikac,² Élisabeth Tronc,³ Mile Ivanda²

¹ Ruđer Bošković Institute, Radiation Chemistry and Dosimetry Laboratory, Bijenička c. 54, Zagreb, Croatia

² Center of Excellence for Advanced Materials and Sensing Devices, Research Unit New Functional Materials, Ruđer Bošković Institute, Bijenička c. 54, Zagreb, Croatia

³ Laboratoire de Chimie de la Matière Condensée, Université Pierre et Marie Curie-Paris6, UMR CNRS 7574 Jussieu, France

* Corresponding author's e-mail address: gotic@irb.hr

RECEIVED: October 23, 2018 * REVISED: January 10, 2019 * ACCEPTED: January 12, 2019

Abstract: Iron/Titanium oxide nanoparticles with initial molar ratio $\text{Fe}/(\text{Fe}+\text{Ti}) = 0.05$ (low loading of Fe in TiO_2) and $\text{Fe}/(\text{Fe}+\text{Ti}) = 0.15$ (high loading of Fe in TiO_2) were synthesized by a modified sol-gel procedure using Ti(IV)-isopropoxide, $\text{FeSO}_4 \cdot 7\text{H}_2\text{O}$ and poly(ethylene glycol) (PEG) as starting material. The amount of doped iron strongly affected structural properties as well as the degree of dispersion of iron in the Fe-Ti-O system. The highly-doped sample contained poorly crystallized hydrated iron(III)-sulphates or basic iron(III)-sulphates in a considerable amount. The lowly-doped Fe- TiO_2 sample contained about 22 wt % of brookite that had taken up iron virtually in the same proportion as anatase. Contrary to quasi-homogeneous distributions of iron in the lowly-doped Fe- TiO_2 sample, the uptake of iron in the highly-doped Fe- TiO_2 sample heated at 500 °C is significant, but anatase is free from iron, thus suggesting a heterogeneous distribution of iron. The photocatalytic activity of the highly-doped Fe- TiO_2 sample was better than that of the lowly-doped Fe- TiO_2 sample, but still below the photoactivity of Degussa P25 reference photocatalyst.

Keywords: TiO_2 , iron-doped, iron/titanium oxide, sol-gel, PEG.

1. INTRODUCTION

FUNCTIONAL properties of advanced ceramics based on TiO_2 (titania) can be improved by a small amount of doping of another element.^[1] A doping element can stabilize TiO_2 component against deterioration of textural properties, most notably the surface area and pore volume, upon thermal treatment. The improved photocatalytic efficiency of iron-doped TiO_2 has been attributed to the action of the iron ions within the TiO_2 matrix inhibiting photogenerated charge pair recombination.^[2,3] Furthermore, the incorporation of iron ions into TiO_2 lattice extended the light absorption and the conversion capacity to the visible portion of the solar spectrum.^[4,5] The iron-doped TiO_2 has attracted much attention due to its improved photocatalytic activity, especially in the more economic production of ammonia from dinitrogen and water vapor at milder temperature and pressure

conditions.^[6,7] The photocatalytic activity, as well as other properties of iron-doped TiO_2 particles, is dependent on its structural and microstructural properties, which can be changed by the synthesis conditions. Generally, the iron-doped samples produced by the precipitation of mixed hydroxides from the solution of inorganic salts, or by hydrolysis from the corresponding alkoxides showed better homogeneity than the samples produced by the impregnation method.

Titanium and iron alkoxides hydrolyze at a relatively same rate, but because of the high cost of iron alkoxides, many researchers combine titanium alkoxide and some inorganic salts of iron in order to obtain iron-doped TiO_2 . The combination of titanium alkoxide and iron acetylacetonate as starting chemicals in the production of iron-doped TiO_2 was also used.^[8-13] The high hydrolysis rate of Ti(IV)-alkoxide as well as of iron ions from inorganic salts, may cause a local uncontrolled precipitation and non-

homogeneous distribution of iron in the TiO₂ matrix. Various polymers, including poly(ethylene glycol) (or shortly PEG), can be used to slow down the hydrolysis rate and to enhance the homogeneous mixing of the metal cations. The advantage in using PEG is mainly due to its very good solubility in polar solvents. PEG influences the hydrolysis primarily by adsorption and steric effect. Iron-doped TiO₂ system is quite complex and its investigations are interesting from the structural standpoint.^[8,10,13-19] The structural complexity of the iron-doped TiO₂ system arises from low solubility limit of iron ions in anatase and rutile, from anatase to rutile transition at higher temperatures and from the appearance of pseudobrookite (Fe₂TiO₅) at higher temperatures and iron loading. Monophasic anatase samples doped with 0.5 to 1 at% of iron showed the best photocatalytic activity within the solubility limit of iron in anatase polymorph. It should be pointed out that the presence of brookite in the iron-doped TiO₂ system and the solubility limit of iron in brookite is not well documented.^[20,21] At higher contents of iron doping, anatase to rutile transition is favored and these samples are virtually photocatalytically inactive. Moreover, at high temperatures only rutile and pseudobrookite are present, both being ineffective photocatalysts. The inactivity of multiphasic solids has been considered in terms of masking of the active phase by surface layers, which create electronic heterojunctions that encourage electron-hole recombination.^[22] Ranjit and Viswanathan^[23] explained the negligible photoactivity of heavily iron-doped TiO₂ by the simple optical screening effect, in which the iron oxide surface phase absorbs all of the electromagnetic radiation and the core phase cannot be activated directly. According to Litter and Navío,^[24] the non-homogeneous distribution of iron in Fe/Ti oxide induced the formation of a second phase such as iron oxide and/or pseudobrookite that acted as a hole trap. The transfer of holes from TiO₂ to Fe₂O₃, as well as rather low mobility of photoexcited electrons, reduces the photoactivity of this catalyst.

In the present work, we focus on the chemical and structural properties of iron/titanium oxide nanosized particles produced by a modified sol-gel method. We tried to favor heterocondensation during the sol-gel synthesis and to stabilize the anatase phase during the thermal treatment of hydro(oxide) precursors. The synthesis was performed using Ti(IV)-isopropoxide, FeSO₄ · 7 H₂O and PEG as starting materials. The usage of iron (II)-sulfate is motivated by the available literature data which suggests that sulfate ions may retard the anatase to rutile transition,^[25] as well as the sintering process during the thermal treatment of hydrous oxide precursor.^[26] Moreover, Rivas *et al.*^[27] found that it is easier to obtain homogeneous samples starting from iron(II)-salt, than with several different iron (III) salts. PEG was added during the

hydrolysis process because its addition before the precipitation is more effective in the modification of the microstructure of the iron-doped TiO₂.^[28] The photocatalytic activities of samples were compared to that of Degussa P25 TiO₂ reference photocatalyst by measuring the formation of CO₂ during the photocatalytic degradation of acetic acid.

2. EXPERIMENTAL

FeSO₄ · 7H₂O, Merck, Ti (IV)-isopropoxide, Aldrich, 97 %, Cat. No. 20,527-3, isopropanol, (Aldrich p.a., poly(ethylene glycol), (PEG), M.W.-15000, Aldrich, Cat. No. 25.885-7, (CH₃)₂C[C₆H₄-4-[OCH₂CH(OH)CH₂(OCH₂CH₂)_nOH]]₂) were used without further purification. Doubly distilled water was used.

Iron-doped TiO₂ nanosized particles with the initial molar ratio of Fe/(Fe+Ti) = 0.05 and 0.15, were synthesized by the modified sol-gel method. Experiments were performed in an oil bath using a specially designed glass apparatus to prevent contact between the precipitation system and moisture from air. Before bubbling N₂ gas into the reaction vessel, extra pure nitrogen (>99.999 N₂) was additionally purified through a pyrogallol and conc. H₂SO₄ bubbler and then through two tubes with silica gel. FeSO₄ · 7H₂O (0.00408 and 0.01227 moles of Fe) was added to Ti(IV)-isopropoxide (0.081 mol of Ti) in isopropanol (75 ml) under nitrogen atmosphere and then hydrolyzed by the addition of poly(ethylene glycol) (PEG) previously dissolved in 120 ml of a doubly distilled water. The suspension in the reaction vessel was refluxed and constantly stirred at 500 to 1000 rpm and after four hours of hydrolysis at 70 °C the obtained suspension was dried in Petri dish at 60 °C. The resulting solid products were denoted as PEG-5 and PEG-15. Samples PEG-15-320, PEG-15-420, PEG15-500, PEG-5-500 and PEG-5-800 were obtained by thermal treatment of as-synthesized sample PEG-5 or PEG-15 in a tubular oven at temperatures 320, 420, 500 and 800 ± 5 °C.

X-ray powder diffraction (XRD) measurements were performed at room temperature using a Philips counter diffractometer (Philips PW 1830) with monochromatic CuK α radiation. The XRD patterns were recorded over the 5–80° 2 θ range with a 2 θ step of 0.05° and a counting time per step of 40 to 60 s. The patterns were analyzed using the Philips PC-APD computing package, which allowed a simultaneous fit of up to 8 lines with a fixed, common pseudo-Voigt line shape. The unit cell parameters were least-squares refined using 7 to 12 lines.

Raman scattering experiments were performed using a standard instrumental technique. A Coherent Innova-100 laser with $\lambda = 514.5$ nm served as an excitation source and the scattered light was analyzed with a DILOR Z-24 Raman spectrometer. The laser power was set at 100 mW at the source.

The Mössbauer spectra were recorded at room temperature using a conventional spectrometer equipped with a source of $^{57}\text{Co}/\text{Rh}$ and operating in the sine velocity mode. The velocities were calibrated from the spectrum of an $\alpha\text{-Fe}$ foil. The isomer shifts, I_S , are given relative to the $\alpha\text{-Fe}$. The spectra of a variety of samples were recorded over a condensed velocity scale ($\pm 10 \text{ mm s}^{-1}$) in order to reveal eventual magnetically split components. Such components were detected in no case. Hence, all detectable phases in the two series of samples are paramagnetic or superparamagnetic at room temperature. The analysis of the spectra was performed by least-squares fitting of a sum of symmetrical doublets of Lorentzian lines. In all cases, satisfactory fits were obtained with two or three quadrupole doublets, which actually model distributions of quadrupole splitting (QS) and, to a lesser extent, of isomer shift.

Proton Induced X-ray Emission (PIXE) was used for the quantitative determination of Fe, Ti and S elements in the iron-doped TiO_2 sample. The measurements were performed using the PIXE facility at the Ruđer Bošković Institute. PIXE analysis showed that the $\text{Fe}/(\text{Fe}+\text{Ti})$ ratios were $\text{Fe}/(\text{Fe}+\text{Ti}) = 0.042$ (2.9 wt% Fe in TiO_2), for relatively low iron-doped sample PEG-5, and $\text{Fe}/(\text{Fe}+\text{Ti})=0.1346$ (9.4 wt% Fe in TiO_2), for relatively highly-doped sample PEG-15, which are slightly below the initial molar ratios of 0.05 and 0.15, respectively. The PIXE quantitative determination of sulfur in sample PEG-15 and in its thermal product at 500 °C showed that the relative amount of sulfur remained constant.

In photocatalytic experiments, Milli-Q water, glacial acetic acid (Kemika, Zagreb), Soda Asbestos millet grains for elementary analysis (Merck), magnesium perchlorate hydrate for elementary analysis (Merck) and Degussa P25 TiO_2 as a standard commercial photocatalyst kindly provided by Degussa-Germany, were used. For the photocatalytic experiments, the as-synthesized samples PEG-5 and PEG-15 were washed with aqueous ammonia, dried overnight at 60 °C and then pressed into tablets and heated at 500 °C. The photocatalytic activity of thus obtained samples, PEG-5-500* and PEG-15-500* was tested by measuring the formation of CO_2 during the photocatalytic mineralization of acetic acid as follows:

25 mg of each sample was ultrasonically dispersed (3 min) in 50 ml of M-Q water. The pH of the suspension was adjusted with the addition of 2 M HCl. 10 ml of suspension was used for pH measuring and the rest of the suspension (40 ml) was transferred into a reaction Pyrex glass flask. Permanent stirring of the suspension was performed from the top of the vessel with a glass stirrer. Spectroscopically pure Hg (Merck) was used to separate the suspension in the reaction flask from the atmosphere. Before bubbling O_2 into the reaction flask, oxygen passed through glass U-tube

with Soda Asbestos grains to purify oxygen from traces of CO_2 and through the trap with M-Q water to obtain water-saturated oxygen stream. Suspensions were purged and continuously stirred in the dark for 10 min and after addition of 1 ml of $1.6 \times 10^{-3} \text{ mol dm}^{-3}$ glacial acetic acid (80 μmol), they were stirred for 20 more minutes. After the equilibration of the system for 30 min in the dark, the suspension was illuminated from the flat polished round bottom (5 cm in diameter) of the Pyrex flask with the white light from homemade 400 W high-pressure mercury lamp. Pyrex glass transmits light longer than 320 nm (checked on UV-visible spectrometer). Two quartz lenses having 3" diameter and 150 mm focus length were used to concentrate the light beams. The CO_2 evolved during irradiation was swept out of the reaction vessel with the stream of oxygen and it was carried to the Heraeus-Quartz glass tube (cat. No. 03579010) filled with Soda Asbestos millet grains for elementary analysis. When reaction gases passed through Soda Asbestos layer, the CO_2 was adsorbed quantitatively and thus separated from the carrier gas. During the experiment, the flow of oxygen was measured and it was about 8 to 10 ml min^{-1} . Soda Asbestos grains were weighed five times before and after the illumination of suspension on Mettler H 54 AR analytical scale so that the difference of mean weighed values gave the quantity of evolved CO_2 . Before passing through the Soda Asbestos grains, reaction gas from the Pyrex flask passed through an empty glass bulb, a bubbler with concentrated H_2SO_4 , U-shaped glass tube with anhydrous CuSO_4 , and a Quartz tube with magnesium perchlorate hydrate for elementary analysis in order to remove any moisture. The same experimental procedure was used for measuring the photocatalytic activity of Degussa P 25 TiO_2 reference photocatalyst.

3. RESULTS AND DISCUSSION

3.1. X-ray Powder Diffraction

Figure 1 shows the XRD patterns of pure poly(ethylene glycol) (PEG). Two of the most intensive lines in the corresponding XRD pattern were located at 23.06 and 19.03° (2θ), and the whole XRD pattern was consistent with the literature data reported for PEG.^[29–31]

Figure 2 shows the XRD patterns of samples PEG-5-500 and PEG-5-800. XRD patterns of the PEG-5-500 powder sample showed the presence of anatase and brookite; $\approx 22\%$ of overall TiO_2 is in the form of brookite. Also, a trace of rutile is detected in the same sample. Table 1 shows $\text{Fe}/(\text{Fe} + \text{Ti})$ molar ratios deduced from PIXE measurements and calculated from the unit-cell parameters of anatase (Table 2) under the procedure given by Schwertmann *et al.*^[32]

The iron/titanium ratio deduced from PIXE measurements and calculated from the parameters of anatase unit cell showed presumably the random

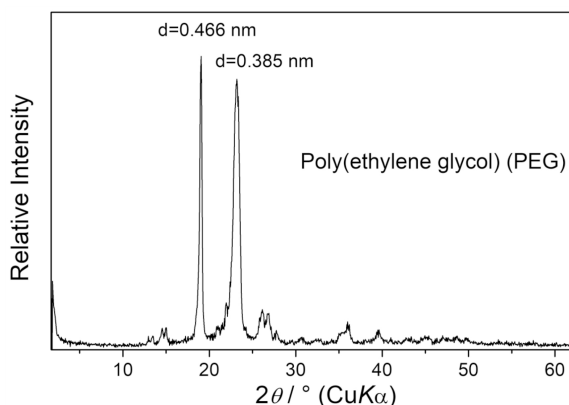


Figure 1. XRD pattern of pure poly(ethylene glycol) (PEG). Two the most intensive lines in the corresponding XRD pattern were located at $d = 0.466$ nm and $d = 0.385$ nm.

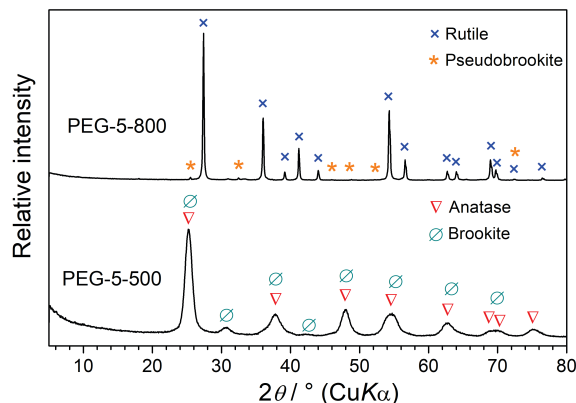


Figure 2. XRD patterns of samples PEG-5-500 and PEG-5-800.

substitutions of Fe for Ti atoms and that the Fe/Ti composition of anatase was the same as that of the whole low-iron doped sample. In the sample PEG-5-500 brookite has taken up iron virtually in the same proportion as

anatase, i.e. $Fe/(Fe + Ti) \approx 0.040$, neglecting the traces of rutile. The cell volume, larger than that of pure brookite by 0.9 %, supports the incorporation of iron in the brookite phase. In octahedral coordination, Fe(III) is bigger than Ti

Table 1. Fe/(Fe+Ti) molar ratio deduced from PIXE measurements and calculated^[27] from the parameters of anatase unit cell (Table 2)

Sample	Anatase unit cell			PIXE	a	c	V
	a / nm	c / nm	V / nm^3				
PEG-5-500	0.3794(1)	0.9504(4)	0.1368(1)	0.040 ^c	0.037 ^a 0.043 ^b	0.075 ^a	0.046 ^a 0.039 ^b
PEG-15-500	0.3785(2)	0.9491(8)	0.1360(3)	0.105	-0.006 ^a -0.003 ^b	0.036 ^a	0.006 ^a -0.017 ^b

^a Synthetic samples: $a = 0.37862 + 0.0210X$; $c = 0.94788 + 0.0338X$; $V = 0.13588 + 0.0200X$.

^b Synthetic and soil samples: $a = 0.37856 + 0.0194X$; $V = 0.13624 + 0.0143X$.

^c Assumed to be the same as for PEG-5.

Table 2. Fitted unit cell parameters of well-identified phases

	PEG-15	-320	-420	-500	PEG-5-500	-800	pure phase ^a
A	a / nm	0.3803(3)	0.3779(3)	0.3800(3)	0.3785(2)	0.3794(1)	0.37852
	c / nm	0.953(1)	0.949(1)	0.951(1)	0.9491(8)	0.9504(4)	0.95139
	V / nm^3	0.1378(3)	0.1355(4)	0.1372(4)	0.1360(3)	0.1368(1)	0.13631
B	a / nm				0.543(2)		0.54558
	b / nm				0.928(3)		0.91819
	c / nm				0.5169(6)		0.51429
	V / nm^3				0.260(2)		0.25763
R	a / nm			0.4582(3)		0.4596(1) ^b	0.45933
	c / nm			0.2969(5)		0.2962(1)	0.29592
	V / nm^3			0.0623(2)		0.0626(1)	0.06243
PB	a / nm					0.9824(6)	0.97965
	b / nm					0.9985(2)	0.99805
	c / nm					0.3730(1)	0.37301
	V / nm^3					0.3660(4)	0.36471

^a JCPDS file: A(21-1272); B(29-1360); R(21-1276); PB(41-1432).

^b Narrow-line component.

Table 3. Unit cell parameters measured for oxide phases in sample PEG-5-800

Phase	Unit cell parameters
R	a = 0.4596(1) nm, c = 0.2962(1) nm (narrow lines)
R	a = 0.4600(2) nm, c = 0.2961(1) nm (broad lines)
PB	a = 1.9824(6) nm, b = 0.9985 nm, c = 0.3730(1) nm

Key: R = rutile; PB=pseudobrookite.

(IV), and the relative increase in ionic radius is $\Delta R/R = 0.07$.^[32] The Vegard law applied to the estimated iron uptake yields an increase in the cell volume $\Delta V/V = 3\Delta R/R \cdot Fe/(Fe + Ti) = 0.008$. Thus, the observed increase of the cell volume may appear consistent with the assumption of random substitution of Fe atoms for Ti ones. However, the increase of the cell volume is basically due to the increase of the *b*-length; the *a*- and *c*-lengths vary only slightly, in opposite ways (Table 2). The large increase of the *b*-length, by 1.06 %, suggests that a distorted structure may form for larger Fe uptakes. On the other hand, there is controversy regarding the size of Fe^{3+} and Ti^{4+} . Shwertmann,^[32] Gennari,^[33] Choi^[5] and Millot^[34] have reported that Fe^{3+} is bigger than Ti^{4+} , whereas Serpone,^[4] Ranjit,^[23] Bally^[35] and Wang^[19] reported that Fe^{3+} is smaller than Ti^{4+} . Millot *et al.*^[34] reported for substitution of Ti for Fe atoms that even the Ti^{4+} ionic radius was smaller than that of Fe^{3+} , the very large oxygen vacancy distance might explain the increase of lattice parameters.

In the PEG-5-500 powder the Fe(III)-oxysulphate phase may also exist, but in a negligible amount from the XRD point of view. We shall focus more on this phase discussing the results obtained with PEG-15 and its thermal evolution products.

XRD patterns of PEG-5-800 powder sample (Figure 2) showed a complete transformation of anatase and brookite polymorphs into rutile. Pseudobrookite, an associated phase to rutile, is also found in the same sample. The volume of the pseudobrookite unit cell is larger than that given in JCPDS 41-1432 by 0.4 %. The actual fraction of pseudobrookite was problematic to estimate, because of the presence of the rutile broad component. If it is neglected, one has found $Ti_{PB}/Ti_R \approx 0.01$, and $Fe_{PB}/Fe_{tot} \approx 0.5$. Some or all of iron may be incorporated in rutile in view of the small increase of the unit cell in volume compared to pure rutile. The unit cell parameters of the oxide phases present in sample PEG-5-800 are given in Table 3.

The pattern analysis of sample PEG-5-800 leads to consider two sets of lines for rutile with similar positions, very different widths and areas in a similar ratio. These suggest a broad (two-mode) distribution of crystallite sizes. The cell volume of rutile is larger than that of the reference (JCPDS 21-1276) by 0.3 % (narrow component) to 0.4 % (broad component).

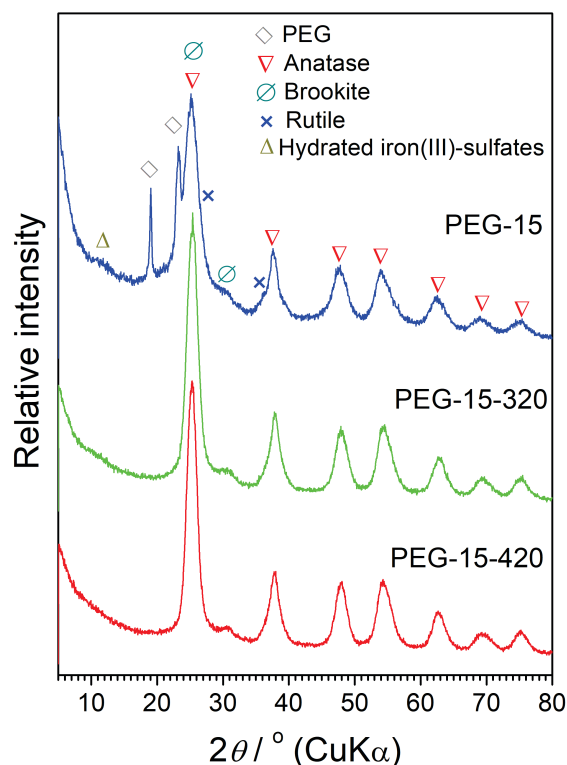
**Figure 3.** XRD patterns of samples PEG-15 (blue), PEG-15-320 (green) and PEG-15-420 (red).

Figure 3 shows the XRD patterns of samples PEG-15, PEG-15-320 and PEG-15-420. In sample PEG-15, XRD found anatase, brookite, crystallized PEG and one additional phase which could be poorly crystallized Fe(III) hydroxysulphate in a relatively significant amount. The characteristic XRD line shift, varying between the samples, suggested structural variations related mostly to dehydration. The major XRD lines of some Fe(III) hydroxysulphates are given in Table 4. After heating the sample PEG-15 at 320 °C, the PEG component burned. XRD showed the same phases in sample PEG-15-420, similar to sample PEG-15-320.

Figure 4 shows the XRD pattern of sample PEG-15-500. In this sample, anatase is the dominant phase, the hydrated iron(III)-sulphates are still present and the formation of rutile and hematite is obvious. Generally, it is known that at this temperature iron(III)-hydroxy or oxysulphates may convert to hematite. Incorporation of a small amount of titanium ions in hematite, as a solid solution, is also possible. In the same sample, the presence of brookite may also be suggested.

The ratios of TiO_2 polymorphs in sample PEG-15-500, A:B:R = 83:11:6 are deduced. Under the used assumptions, hematite involves 10 % of the iron in the sample. However, taking into account differences in line width between

Table 4. Major lines of some hydrated iron(III) sulphates and basic iron(III) sulphates

JCPDS	'FeOS'	<i>d</i> / nm	<i>l</i>						
44-1425	Fe ₂ (SO ₄) ₃ ·9H ₂ O	0.828	75	0.364	62	0.336	100	0.276	81
29-714	Fe _{4.67} (SO ₄) ₆ ·20H ₂ O	0.906	100	0.558	80	0.358	80	0.353	70
17-155	Fe ₂ (SO ₄) ₂ (OH) ₂ ·7H ₂ O	1.04	60	0.869	80	0.792	100	0.346	60
17-158, 27-249	Fe(SO ₄)(OH)·3H ₂ O	1.13	100	0.869	100	0.357	80	0.305	80
21-429	Fe ₄ (OH) ₁₀ (SO ₄)	0.803	100	0.438	30				

Table 5. Integral widths of the main lines of anatase

	<i>hkl</i>	101	004	200	105	211	204
	sinθ(± 0.0015)	0.219	0.324	0.406	0.454	0.462	0.520
PEG-15	<i>B</i> (° 2θ)	2.8	1.7	3.0	2.0	3.4	3.5
	<i>B</i> cosθ	2.7	1.6	2.7	1.8	3.0	3.0
PEG-15-320	<i>B</i> (° 2θ)	2.3	1.6	2.6	2.0	3.0	2.8
	<i>B</i> cosθ	2.2	1.5	2.4	1.8	2.7	2.4
PEG-15-420	<i>B</i> (° 2θ)	2.0	1.8	2.4	1.8	3.0	2.7
	<i>B</i> cosθ	2.0	1.7	2.2	1.6	2.7	2.3
PEG-15-500	<i>B</i> (° 2θ)	1.2	1.2	1.4	1.4	1.5	1.6
	<i>B</i> cosθ	1.2	1.1	1.3	1.2	1.3	1.4
PEG-5 -00	<i>B</i> (° 2θ)	1.4 ^a	1.7	1.7	1.7	1.9	2.0
	<i>B</i> cosθ	1.4	1.6	1.5	1.7	1.7	1.7

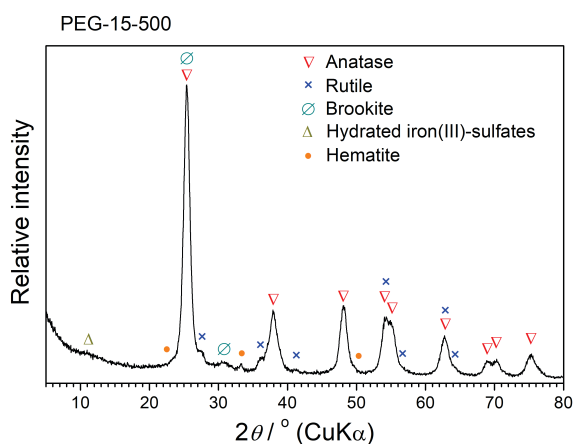
^a Brookite contribution to the observed peak not deduced.

hematite and other three TiO₂ polymorphs it can be concluded that hematite is actually present in a very small amount. The estimated R:A and B:R proportions are in very good agreement with experimental determination found previously.^[36]

Analysis of main XRD lines of anatase component showed that variation of *B*cosθ, as a function of *B*sinθ (Table 5), is not monotonous. If we exclude the 101 line, whose apparent width may be influenced by extrinsic factors (PEG, sulfate phases ...), it is clear that *B*cosθ increases with *h*₂ + *k*₂, virtually independently of *l*. This cannot be explained by an eventual anisotropic morphology, because of tetragonal structure. It indicates

either an important disorder in the (a,b) plane or the occurrence of additional scattering features.

The dispersion between the *B*cosθ values reduced from PEG-15 to PEG-15-320 and PEG-15-420. Assuming that the broadening of the 004 line is solely due to the small size of anatase crystal (instrumental broadening is negligible), and applying the Scherrer formula $L = \lambda \times 180 / (\pi \times B \cos \theta)$, an apparent crystal size *L* = 5.5 nm (PEG-15), 5.9 nm (PEG-15-320) and 5.2 nm (PEG-15-420), i.e. ≈ 5.5 ± 0.5 nm for the three samples in the *c*-direction was deduced. The main differences between the samples are not related to variations in the crystal size (at least along the *c*-direction), but to variations in the apparent "disorder" effect. For PEG-15-500, the "disorder" effect is reduced compared to PEG-15-420. From the 004 line width, the grain size *L* = 8 nm is calculated. The crystal size is increased by nearly 50 %, volume by a factor of 2 assuming spheres. In contrast to this result, for PEG-5-500 the "disorder" effect is practically negligible. The apparent crystal size is ≈ 5.5 nm and it is significantly smaller than in PEG-15-500.

**Figure 4.** XRD pattern of sample PEG-15-500.

3.2. Raman Spectroscopy

The application of Raman spectroscopy in the monitoring of the crystallization of amorphous titania gel into anatase and the phase conversion, anatase → rutile, has been reported.^[37] Iida *et al.*^[38] also used Raman spectroscopy to monitor the crystallization of amorphous titania gel into anatase. The shifts and broadening of Raman lines in the spectra of nanophase TiO₂ were investigated as a function

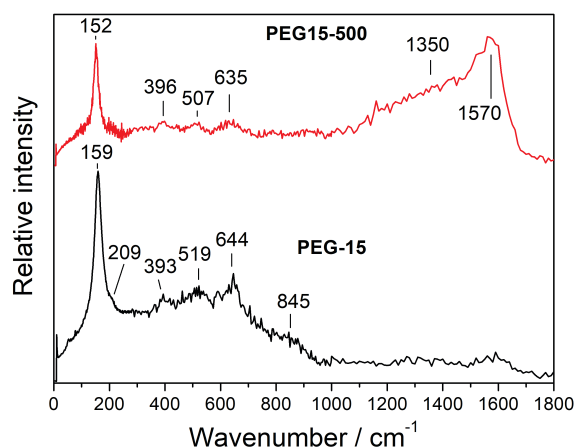


Figure 5. Raman spectra of samples PEG-15 and PEG-15-500.

of annealing at temperatures up to 600 °C in argon or air. Parker and Siegel^[39] explained the shift to higher wavenumbers of the Raman band at 144 cm⁻¹ in nanosized TiO₂ by intergrain defects due to oxygen deficiency, i.e. nanosized TiO₂ was, on average, nonstoichiometric. Kelly *et al.*^[40] reported the application of Raman scattering as a probe to follow the structural evolution of TiO₂ aerogels. It was found that with a decrease in nanoparticle size of TiO₂ the E_g anatase peaks at 142 and 630 cm⁻¹ broadened asymmetrically (high frequencies), shifted to higher wavenumbers and decreased in their intensities. These effects were much more pronounced for the Raman peak at 142 cm⁻¹. Bersani *et al.*^[41] applied the phonon confinement model to explain the dependence of broadening and blueshift of 144 cm⁻¹ Raman peak with a decrease of anatase nanosized particle. In addition to the phonon confinement, nonstoichiometry and pressure effect on the grains, disorder induced by minor phases and defects induced by the presence of organic residues, even after prolonged heat treatment, could cause the shift and the broadening of anatase Raman lines. Ivanda *et al.*^[42] applied the phonon confinement model for the determination of TiO₂ nanoparticle size distributions.

Figure 5 shows the Raman spectra in the wave number range of 1800 to 30 cm⁻¹ of the relatively highly-doped sample and its thermal product at 500 °C, samples PEG-15 and PEG-15-500, respectively. The band at 159 cm⁻¹ with the full width at half maximum (FWHM) of 27 cm⁻¹ recorded for sample PEG-15, corresponds to E_g Raman active mode of anatase. In bulk anatase (or in single crystal anatase), this band is centered at 142 cm⁻¹ and the FWHM has a value of 7 to 8 cm⁻¹. The frequency blue shift of 17 cm⁻¹ (142 to 159 cm⁻¹) and the line broadening of about 19 cm⁻¹ (from 8 to 27 cm⁻¹) for anatase E_g mode in sample

PEG-15 could be attributed mainly to a phonon confinement effect and to a less extent to the disorders and defects induced by the presence of minor phases (brookite and poorly crystallized basic iron sulfate as identified by XRD) and by the presence of residual organic phases. The presence of strain and defects in the samples could have also affected the background intensity in the recorded spectra.^[43,44] It should be pointed out that the position of anatase band at 142 cm⁻¹ could be considerably influenced by a very strong brookite Raman band^[39] at 153 cm⁻¹. However, after thermal treatment of sample PEG-15 at 500 °C, the band at 159 cm⁻¹ shifted to 152 cm⁻¹ and FWHM decreased from 27 to 23 cm⁻¹ in spite of the fact that there were no changes in the relative concentration of brookite before and after thermal treatment (XRD results). Also, the relative Raman shift to the lower wave numbers and the decrease of FWHM of anatase E_g mode with thermal treatment of sample PEG-15 matched very well with XRD results that showed the increase of particle size from 5.5 nm in sample PEG-15 to 8 nm in sample PEG-15-500. Two lines in the Raman spectrum of sample PEG-15-500 at 1350 and very intensive and broad band at 1570 cm⁻¹ could be assigned to the G and D lines of pre-graphitized carbon. The origin of these two lines was due to carbon formed during the decomposition of organic phase present in sample. The three lines in the region from 390 cm⁻¹ to 650 cm⁻¹ might be attributed to the vibrations of sulfate anions.^[45]

In a previous work^[46] we proposed for the first time the method of low-frequency Raman scattering in particle size determination of nanosized TiO₂. The particle size determination by this method was compared with HREM, XRD and SAXS, and a good agreement in the results between these methods was achieved.^[47-51] Moreover, Ivanda *et al.*^[42,51] showed that low-frequency Raman scattering could be applied in the determination of nanoparticle size distribution. The comparison of nanoparticle size distributions obtained by two complementary techniques, low-frequency Raman scattering (LFR) and High-resolution transmission electron microscopy (HREM), could be found elsewhere.^[51]

Figure 6 shows particle size distribution of samples PEG-15 and PEG-15-500 based on low-frequency Raman spectroscopy. according to the procedure by Ivanda *et al.*^[50] Both samples contain very small nanoparticles, but PEG-15-500 sample had slightly larger particles than sample PEG-15 because of the thermal treatment at 500 °C.

3.3 Mössbauer Results

The results of Mössbauer spectroscopic measurements at room temperature (RT) are summarized in Figures 7 and 8, and Table 6.

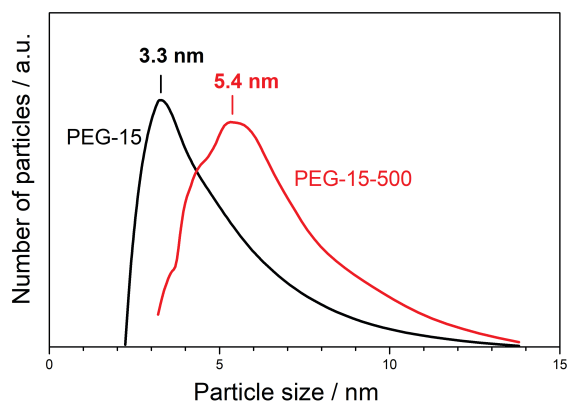


Figure 6. Particle size distribution of samples PEG-15 and PEG-15-500 based on low-frequency Raman spectroscopy.

Mössbauer spectra were considered as a superposition of two or more doublets. After heating the sample PEG-5 at 420 °C, a pronounced asymmetric broadening in the Mössbauer spectrum was observed, and this spectrum was fitted as the superposition of two doublets with the splitting 0.50 and 1.12 mm s⁻¹. The corresponding areas under the peaks are 55 and 45 %, respectively. The spectral component with the splitting

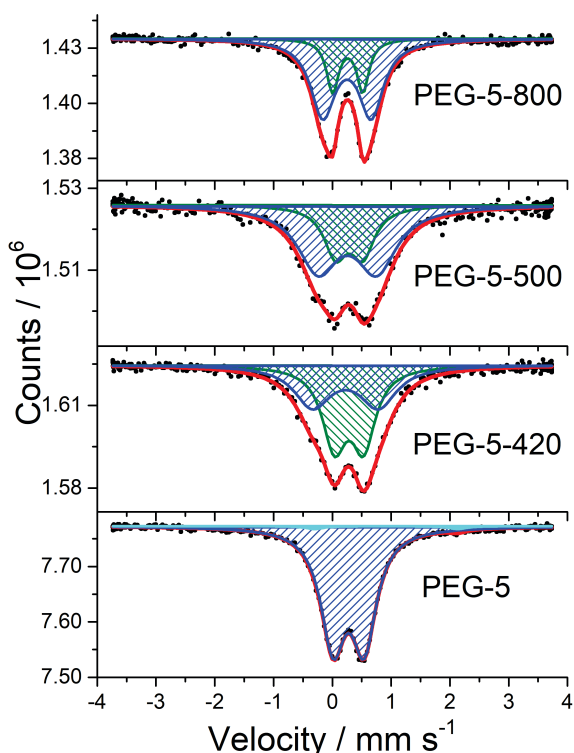


Figure 7. Results of Mössbauer spectroscopic measurements at room temperature of sample PEG-5 and its thermal treatment products.

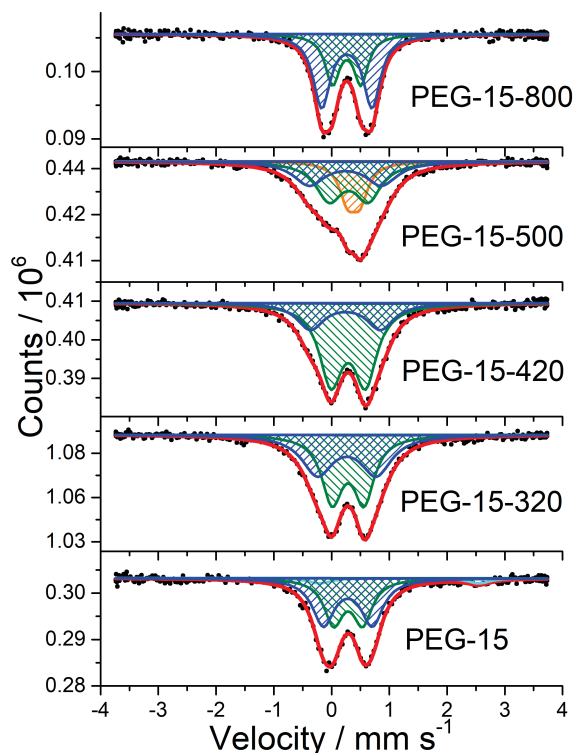


Figure 8. Results of Mössbauer spectroscopic measurements at room temperature of sample PEG-15 and its thermal treatment products.

1.12 mm s⁻¹ can be assigned to basic iron(III) sulfate phase with varying stoichiometry. The presence of basic iron(III) sulfate phase can be considered also in sample PEG-5-500. Significant variations in quadrupole splittings, which are generally observed in the studies of basic iron(III) sulfates indicate different stoichiometries of these compounds,^[52-54] although some authors argue that variations in quadrupole splittings emerge from differences in the electric field symmetry. These differences can arise from adsorption of iron-containing particles on a support surface, symmetry distortion or loss of water from the second coordination sphere during adsorption.^[55-58] The presence of some kind of hydrated and poorly crystallized basic iron(III) sulfate cannot be ruled out even in the starting sample PEG-5. After heating the sample PEG-5 up to a maximum temperature of 800 °C (PEG-5-800), the superposition of two quadrupole doublets with the splittings 0.51 and 0.82 mm s⁻¹, respectively, were obtained. These values and other parameters indicate the phase difference between this sample and the previous two (PEG-5-420 and PEG-5-500). Evidently, PEG-5-800 is free from a sulfate-bearing phase. In this sample, iron is presumably distributed between pseudobrookite, iron titanate and eventually rutile.

Table 6. ^{57}Fe Mössbauer parameters recorded at room temperature for samples PEG-5 and PEG-15 and their thermal products heated at 320, 420, 500 and 800 °C. The isomer shifts, IS, are given relative to the α -Fe foil

Sample	IS/ mms ⁻¹	QS/ mms ⁻¹	W/ mms ⁻¹	A	Sample	IS/ mms ⁻¹	QS/ mms ⁻¹	W/ mms ⁻¹	A
PEG-15	0.29	0.50	0.40	0.42	PEG-5	0.28	0.53	0.51	0.98
	0.28	0.84	0.46	0.51		0.91	2.43	0.35	0.02
	1.17	2.76	0.49	0.07					
PEG-15-320	0.29	0.55	0.43	0.52					
	0.26	1.02	0.65	0.48					
PEG-15-420	0.29	0.60	0.48	0.71	PEG-5_420	0.28	0.50	0.49	0.55
	0.24	1.21	0.57	0.29		0.22	1.12	0.75	0.45
PEG-15-500	0.38	0.21	0.34	0.25	PEG-5_500	0.29	0.46	0.48	0.31
	0.30	0.67	0.56	0.43		0.26	1.00	0.83	0.69
	0.24	1.25	0.65	0.32					
PEG-15-800	0.26	0.49	0.30	0.36	PEG-5_800	0.26	0.51	0.25	0.26
	0.26	0.87	0.36	0.64		0.25	0.82	0.50	0.74

On the basis of the Mössbauer spectra of samples PEG-15 to PEG-15-500, it is estimated that at least 60 % of iron is engaged in a sulfato phase. Evolution of this phase with increasing the temperature is reflected in the shape of the corresponding spectra. Generally, the lower the heating temperature of the sample the higher the content of H₂O is (bonded or hydrated) in basic iron(III) sulfates. As it has been already mentioned, these structural variations between samples show differences in quadrupole splittings. Thus, we can assign the component with the splitting ≈ 0.84 to ≈ 1 mm s⁻¹ to Fe³⁺ ions in the sulfate phase with varying stoichiometry, Fe(OH)_x(SO₄)_y zH₂O, where x, y and z are variable. The similarity of the relative areas of (i) the pair of component (QS ≈ 0.2 and ≈ 1.3 mm s⁻¹) for PEG-15-500, (ii) the component with QS ≈ 1 mm s⁻¹ for PEG-15-320, and (iii) the pair of component due to Fe(III) with QS = 0.85 mm s⁻¹ and to Fe(II) in PEG-15 supports previous conclusions.

The assignment of the component with QS ≈ 0.5 mm s⁻¹ in PEG-15, possibly correlated with that of QS ≈ 0.7 mm s⁻¹ in PEG-15-500, is ambiguous. Rather small distribution of the environment can be found in strongly hydroxylated or hydrated sulfates, as well as in a variety of materials, including the PEG environment. In PEG-15-800 almost all iron is incorporated in pseudobrookite. Finally, it can be concluded that major differences between the sets of samples (PEG-5 and PEG-15 series) are possibly due to different degrees of dispersion of iron in initial materials, quasi-homogeneous in PEG-5 and heterogeneous in PEG-15. On the other hand, similarities were mainly influenced by the presence of sulfate-bearing phases, which influenced the evolution of the oxide phase during the thermal treatment, and consequently the corresponding spectra.

3.4. Photocatalytic Measurements

The photocatalytic activity of sol-gel synthesized samples was compared with the photocatalytic activity of Degussa P25 TiO₂ reference photocatalyst. The photocatalytic activities of samples and Degussa P25 TiO₂ were tested by measuring the formation of CO₂ during the complete mineralization of acetic acid as a model organic pollutant in wastewaters. The formation of CO₂ was measured because the key parameter in the destruction of organics in water is the rate of CO₂ formation and not the rate of disappearance of the organic compound.^[59,60] Table 7 shows the results of measured photocatalytic activities of samples PEG-5-500* and PEG-15-500* relative to the Degussa P25 TiO₂ standard photocatalyst. Samples used in photocatalytic experiments were washed with aqueous ammonia before their sintering at 500 °C because Ito *et al.*^[61] showed that washing TiO₂ particles with aqueous ammonia before sintering was very effective for cleaning their surface from adsorbed SO₄²⁻ ions. Generally, photocatalytic activity is significantly influenced by the synthesis procedure, crystal phase composition, degree of crystallinity and by the amount of surface OH groups. Degussa P25 TiO₂ is a non-porous 70–80 : 30–20 % anatase to rutile mixture with crystallite sizes of ≈ 30 nm in 0.1 to 0.2 μm diameter aggregates.^[62–64] Relative photonic efficiencies^[60,65–67] for the degradation of phenol in the presence of various commercially available TiO₂ sources and in the presence of Degussa P25 TiO₂ was reported by Serpone *et al.*^[66] and Bockelmann *et al.*^[68] Lindner *et al.*^[69] reported that the same photocatalyst can exhibit rather different photocatalytic efficiencies when different model pollutants were employed. Also, the photocatalyst concentration in the suspension can affect the efficiency of the degradation. For example, Bockelmann *et al.*^[68]

Table 7. Photocatalytic activities of samples PEG-5-500 and PEG-15-500 compared with the photocatalytic activity of Degussa P25 TiO₂ standard photocatalyst. Photoactivity was obtained by measuring the formation of CO₂ during the complete mineralization of acetic acid as a model organic pollutant in wastewaters

Source of TiO ₂	Volume of suspension /ml	c(TiO ₂) /g L ⁻¹	Volume of added acetic acid**/ml	pH of suspension before irradiation	Formed CO ₂ *** /mg	Photocatalytic activity relative to P25 TiO ₂
Degussa P25	40	0.5	1	2.6	1.11	1.00
PEG-5-500*	40	0.5	1	2.8	0.15	0.13
PEG-15-500*	40	0.5	1	3.2	0.58	0.52

* As synthesized samples PEG-5 and PEG-15 were washed in aqueous ammonia before their sintering at 500 °C. The amount of iron in TiO₂ corresponded to 2.9 and 9.4 wt% of iron for PEG-5-500 and PEG-15-500 samples, respectively. **The concentration of glacial acetic acid was 1.6·10⁻³ mol dm⁻³, so that the addition of 1 ml corresponded to the addition of 80 μmol. ***Samples were illuminated with 400 W high-pressure mercury lamp for six hours. O₂ was used as a carrier gas with the flow rate of about 8–10 ml min⁻¹. The experimental procedure for the determination of CO₂ was given in experimental part of this work.

showed that the optimal catalyst concentration for degradation of dichloroacetic acid (DCA) was 0.5 g L⁻¹ for Degussa P25 TiO₂ and 5.0 g L⁻¹ for commercially available TiO₂ photocatalyst, Hombikat UV 100.

Bahnemann *et al.*^[70] synthesized colloidal Ti/Fe mixed oxide nanoparticles with Fe³⁺ content varying from 0.05 up to 50 at% and particle diameter between 4–6 nm. The photocatalytic activity of these Ti/Fe mixed oxide particles was compared to that of pure colloidal TiO₂ and it was found that the efficiency of the destruction of the model pollutant dichloroacetic acid obtained with the Ti/Fe-mixed oxide particles was always higher than that of pure TiO₂ colloids. Ti/Fe mixed oxide sample with 2.5 at% Fe³⁺ showed the maximum photocatalytic activity. Contrary to these results, Navío *et al.*^[71] reported lower photocatalytic activity for sol-gel synthesized iron-doped TiO₂ samples compared to the undoped sample for photodegradation of EDTA and for the photocatalytic reduction of Cr(VI). In addition, the photocatalytic activity of iron-doped sol-gel samples was much lower than the activity of Degussa P25 TiO₂. The lower photocatalytic activity of iron-doped samples was attributed to the larger amount of defects introduced by the sol-gel synthesis as well as to the presence of carbon impurities remaining after the thermal decomposition of the organic precursor. In this work, the photocatalytic activity of the TiO₂ sample with higher iron doping was better than that of the TiO₂ sample with lower iron doping, but still much less than the photoactivity of Degussa P25 TiO₂ (Table 7).

CONCLUSIONS

Iron/titanium nanoparticles were synthesized by a modified sol-gel procedure using Ti(IV)-isopropoxide, FeSO₄ · 7H₂O and poly(ethylene glycol) (PEG) as starting materials. It was found that the parameters during the sol-gel synthesis, such as pH, the presence of PEG and the

choice of the iron precursor, as well as the amount of added iron, strongly affected the structural properties and the degree of dispersion of iron in the Fe-Ti-O system. The iron/titanium ratio deduced from PIXE measurements and calculated from the parameters of anatase unit cell showed presumably the random substitution of Fe for Ti atoms. Furthermore, the Fe/(Fe+Ti) ratio in anatase was the same as that of the whole TiO₂ sample with lower iron doping (2.9 wt% of Fe). It was shown that about 22 wt% of brookite present in the TiO₂ sample with lower iron doping incorporates iron virtually in the same proportion as anatase. Contrary to quasi-homogeneous distributions of iron in samples with relatively lower doping of iron, the uptake of iron in the samples with relatively higher doping of iron (9.4 wt% of Fe) heated at 500 °C is significant. However, anatase is free from iron thus suggesting heterogeneous distributions of iron in this sample. At least 60 % of the iron in TiO₂ sample with higher iron doping and in its thermal product at 500 °C is in the form of sulfato phases. The photocatalytic activity of TiO₂ sample with higher iron doping (9.4 wt% of Fe) was better than that of TiO₂ sample with lower iron doping (2.9 wt% of Fe), but still less than the photoactivity of Degussa P25 photocatalyst.

Acknowledgment. This work has been fully supported by a project co-financed by the Croatian Government and the European Union through the European Regional Development Fund - the Competitiveness and Cohesion Operational Programme (KK.01.1.1.01.0001).

REFERENCES

- [1] D.-S. Bae, K.-S. Han, S.-H. Choi, *Solid State Ionics* **1998**, *109*, 239.
- [2] J. Moser, M. Grätzel, R. Gallay, *Helv. Chim. Acta* **1987**, *70*, 1596.
- [3] M. Grätzel, in *Photocatalysis: Fundamentals and Applications*, Vol. 1 (Eds.: N. Serpone, E. Pelizzetti), Wiley-Interscience, New York, **1989**, p. 650.

- [4] N. Serpone, D. Lawless, J. Disdier, J.-M. Herrmann, *Langmuir* **1994**, *10*, 643.
- [5] W. Choi, A. Termin, M. R. Hoffmann, *J. Phys. Chem.* **1994**, *98*, 13669.
- [6] G. N. Schrauzer, T. D. Guth, *J. Am. Chem. Soc.* **1977**, *99*, 7189.
- [7] J. Soria, J. C. Conesa, V. Augugliaro, L. Palmisano, M. Schiavello, A. Sclafani, *J. Phys. Chem.* **1991**, *95*, 274.
- [8] P. Guglielmi, P. Colombo, *Ceram. Acta* **1989**, *1*, 19.
- [9] P. Colombo, M. Guglielmi, S. Enzo, *J. Eur. Ceram. Soc.* **1991**, *8*, 383.
- [10] M. V. Tsodikov, O. V. Bukhtenko, O. G. Ellert, V. M. Shcherbakov, D. I. Kochubey, *J. Mater. Sci.* **1995**, *30*, 1087.
- [11] J. Navío, G. Colón, M. I. Litter, G. N. Bianco, *J. Mol. Catal. A Chem.* **1996**, *106*, 267.
- [12] J. A. Navío, G. Colón, M. Trillas, J. Peral, X. Domènech, J. J. Testa, J. Padrón, D. Rodríguez, M. I. Litter, *Appl. Catal. B Environ.* **1998**, *16*, 187.
- [13] J. A. Navío, G. Colón, M. Macías, C. Real, M. I. Litter, *Appl. Catal. A Gen.* **1999**, *177*, 111.
- [14] D. Cordischi, N. Burriesci, F. D'Alba, M. Petrera, G. Polizzotti, M. Schiavello, *J. Solid State Chem.* **1985**, *56*, 182.
- [15] R. I. Bickley, J. S. Lees, R. J. D. Tilley, L. Palmisano, M. Schiavello, *J. Chem. Soc. Faraday Trans.* **1992**, *88*, 377.
- [16] J. A. Navío, M. Macías, M. González-Catalán, A. Justo, *J. Mater. Sci.* **1992**, *27*, 3036.
- [17] M. Maček, B. Orel, T. Meden, *J. Sol-Gel Sci. Technol.* **1997**, *8*, 771.
- [18] B. Pal, M. Sharon, G. Nogami, *Mater. Chem. Phys.* **1999**, *59*, 254.
- [19] Y. Wang, H. Cheng, Y. Hao, J. Ma, W. Li, S. Cai, *J. Mater. Sci.* **1999**, *34*, 3721.
- [20] A. Golubović, M. Šćepanović, A. Kremenović, S. Aškračić, V. Berec, Z. Dohčević-Mitrović, Z. V. Popović, *J. Sol-Gel Sci. Technol.* **2009**, *49*, 311.
- [21] M. Grujić-Brojčin, S. Armaković, N. Tomić, B. Abramović, A. Golubović, B. Stojadinović, A. Kremenović, B. Babić, Z. Dohčević-Mitrović, M. Šćepanović, *Mater. Charact.* **2014**, *88*, 30.
- [22] R. I. Bickley, T. Gonzalez-Carreño, A. R. Gonzalez-Elipé, G. Munuera, L. Palmisano, *J. Chem. Soc. Faraday Trans.* **1994**, *90*, 2257.
- [23] K. T. Ranjit, B. Viswanathan, *J. Photochem. Photobiol. A Chem.* **1997**, *108*, 79.
- [24] M. I. Litter, J. A. Navío, *J. Photochem. Photobiol. A Chem.* **1994**, *84*, 183.
- [25] V. T. Zaspalis, W. Van Praag, K. Keizer, J. R. H. Ross, A. J. Burggraaf, *J. Mater. Sci.* **1992**, *27*, 1023.
- [26] X. Fu, W. A. Zeltner, Q. Yang, M. A. Anderson, *J. Catal.* **1997**, *168*, 482.
- [27] A. B. Rives, T. S. Kulkarni, A. L. Schwaner, *Langmuir* **1993**, *9*, 192.
- [28] T. Klimova, E. Carmona, J. Ramirez, *J. Mater. Sci.* **1998**, *33*, 1981.
- [29] W. H. Barnes, S. Ross, *J. Am. Chem. Soc.* **1936**, *58*, 1129.
- [30] H. Tadokoro, *J. Polym. Sci. Part C Polym. Symp.* **2007**, *15*, 1.
- [31] B. Wunderlich, *Macromolecular Physics*, Academic Press, New York, **1973**, p. 119.
- [32] U. Schwertmann, J. Friedl, G. Pfab, A. U. Gehring, *Clays Clay Miner.* **1995**, *43*, 599.
- [33] F. C. Gennari, D. M. Pasquevich, *J. Mater. Sci.* **1998**, *33*, 1571.
- [34] N. Millot, S. Begin-Colin, P. Perriat, G. Le Caër, *J. Solid State Chem.* **1998**, *139*, 66.
- [35] A. R. Bally, E. N. Korobeinikova, P. E. Schmid, F. Lévy, F. Bussy, *J. Phys. D. Appl. Phys.* **1998**, *31*, 1149.
- [36] N. Šijaković-Vujičić, M. Gotić, S. Musić, M. Ivanda, S. Popović, *J. Sol-Gel Sci. Technol.* **2004**, *30*, 5.
- [37] K. Terabe, K. Kato, H. Miyazaki, S. Yamaguchi, A. Imai, Y. Iguchi, *J. Mater. Sci.* **1994**, *29*, 1617.
- [38] Y. Iida, M. Furukawa, K. Kato, H. Morikawa, *Appl. Spectrosc.* **1997**, *51*, 673.
- [39] J. C. Parker, R. W. Siegel, *J. Mater. Res.* **1990**, *5*, 1246.
- [40] S. Kelly, F. H. Pollak, M. Tomkiewicz, *J. Phys. Chem. B* **1997**, *101*, 2730.
- [41] D. Bersani, P. P. Lottici, X.-Z. Ding, *Appl. Phys. Lett.* **1998**, *72*, 73.
- [42] M. Ivanda, S. Musić, M. Gotić, A. Turković, A. M. Tonejc, O. Gamulin, *J. Mol. Struct.* **1999**, *480–481*, 641.
- [43] A. Kremenović, B. Antić, J. Blanuša, M. Čomor, P. Colombar, L. Mazerolles, E. S. Bozin, *J. Phys. Chem. C* **2011**, *115*, 4395.
- [44] A. Kremenović, M. Grujić Brojcin, A.-M. Welsch, P. Colombar, *J. Appl. Crystallogr.* **2013**, *46*, 1874.
- [45] R. L. Frost, Y. Xi, R. Scholz, A. López, A. Granja, *Spectrochim. Acta Part A Mol. Biomol. Spectrosc.* **2013**, *109*, 201.
- [46] M. Gotić, M. Ivanda, A. Sekulić, S. Musić, S. Popović, A. Turković, K. Furić, *Mater. Lett.* **1996**, *28*, 225.
- [47] S. Musić, M. Gotić, M. Ivanda, S. Popović, A. Turković, R. Trojko, A. Sekulić, K. Furić, *Mater. Sci. Eng. B* **1997**, *47*, 33.
- [48] A. Turković, M. Ivanda, S. Popović, A. Tonejc, M. Gotić, P. Dubček, S. Musić, *J. Mol. Struct.* **1997**, *410–411*, 271.
- [49] M. Gotić, M. Ivanda, S. Popović, S. Musić, A. Sekulić, A. Turković, K. Furić, *J. Raman Spectrosc.* **1997**, *28*, 555.
- [50] M. Ivanda, S. Musić, S. Popović, M. Gotić, *J. Mol. Struct.* **1999**, *480–481*, 645.

- [51] M. Ivanda, K. Furić, S. Musić, M. Ristić, M. Gotić, D. Ristić, A. M. Tonejć, I. Djerdj, M. Mattarelli, M. Montagna, F. Rossi, M. Ferrari, A. Chiasera, Y. Jestin, G. C. Righini, W. Kiefer, R. R. Gonçalves, *J. Raman Spectrosc.* **2007**, *38*, 647.
- [52] P. K. Gallagher, D. W. Johnson, F. Schrey, *J. Am. Ceram. Soc.* **1970**, *53*, 666.
- [53] B. D. Rumbold, G. V. H. Wilson, *J. Phys. Chem. Solids* **1974**, *35*, 241.
- [54] A. R. Champion, R. W. Vaughan, H. G. Drickamer, *J. Chem. Phys.* **1967**, *47*, 2583.
- [55] A. A. Kamnev, A. A. Smekhnov, *Anal. Bioanal. Chem.* **1996**, *355*, 710.
- [56] A. A. Kamnev, Y. D. Perfilyev, *J. Radioanal. Nucl. Chem. Artic.* **1995**, *190*, 321.
- [57] A. A. Kamnev, M. Ristić, V. Angelov, *J. Mol. Struct.* **1995**, *349*, 77.
- [58] A. A. Kamnev, B. B. Ezhov, V. Rusanov, V. Angelov, *Electrochim. Acta* **1992**, *37*, 469.
- [59] R. W. Matthews, *Water Res.* **1990**, *24*, 653.
- [60] N. Serpone, R. Terzian, D. Lawless, P. Kennepohl, G. Sauvé, *J. Photochem. Photobiol. A Chem.* **1993**, *73*, 11.
- [61] S. Ito, S. Inoue, H. Kawada, M. Hara, M. Iwasaki, H. Tada, *J. Colloid Interface Sci.* **1999**, *216*, 59.
- [62] R. I. Bickley, T. Gonzalez-Carreno, J. S. Lees, L. Palmisano, R. J. D. Tilley, *J. Solid State Chem.* **1991**, *92*, 178.
- [63] A. K. Datye, G. Riegel, J. R. Bolton, M. Huang, M. R. Prairie, *J. Solid State Chem.* **1995**, *115*, 236.
- [64] A. Fernández-Nieves, C. Richter, F. J. de las Nieves, *An. Fis.* **1998**, *94*, 84.
- [65] A. Salinaro, A. V. Emeline, J. Zhao, H. Hidaka, V. K. Ryabchuk, N. Serpone, *Pure Appl. Chem.* **1999**, *71*, 321.
- [66] N. Serpone, G. Sauvé, R. Koch, H. Tahiri, P. Pichat, P. Piccinini, E. Pelizzetti, H. Hidaka, *J. Photochem. Photobiol. A Chem.* **1996**, *94*, 191.
- [67] N. Serpone, *J. Photochem. Photobiol. A Chem.* **1997**, *104*, 1.
- [68] D. Bockelmann, M. Lindner, D. Bahnemann, in *Fine Particles Science and Technology*, Vol. 5 (Ed.: E. Pelizzetti), Springer Netherlands, **1996**, pp. 675–689.
- [69] M. Lindner, D. W. Bahnemann, B. Hirthe, W.-D. Griebler, *J. Sol. Energy Eng.* **1997**, *119*, 120.
- [70] D. W. Bahnemann, *Res. Chem. Intermed.* **2000**, *26*, 207.
- [71] J. A. Navío, J. J. Testa, P. Djedjeian, J. R. Padrón, D. Rodríguez, M. I. Litter, *Appl. Catal. A Gen.* **1999**, *178*, 191.